

MASSIVE STAR FORMATION IN METAL-ENRICHED HALOES AT HIGH REDSHIFT

JOHN A. REGAN^{1,*}, ZOLTÁN HAIMAN², JOHN H. WISE³, BRIAN W. O'SHEA^{4,5,6,7}, AND MICHAEL L. NORMAN⁸¹Department of Theoretical Physics, Maynooth University, Maynooth, Ireland²Department of Astronomy, Columbia University, 550 W. 120th Street, New York, NY 10027, USA³Center for Relativistic Astrophysics, Georgia Institute of Technology, 837 State Street, Atlanta, GA 30332, USA⁴Department of Computational Mathematics, Science, and Engineering, Michigan State University, MI, 48823, USA⁵Department of Physics and Astronomy, Michigan State University, MI, 48823, USA⁶Joint Institute for Nuclear Astrophysics - Center for the Evolution of the Elements, USA⁷National Superconducting Cyclotron Laboratory, Michigan State, University, MI, 48823, USA and⁸Center for Astrophysics and Space Sciences, University of California, San Diego, 9500 Gilman Dr, La Jolla, CA 92093

Version January 17, 2022

ABSTRACT

The formation of supermassive stars has generally been studied under the assumption of rapid accretion of pristine metal-free gas. Recently it was found, however, that gas enriched to metallicities up to $Z \sim 10^{-3} Z_{\odot}$ can also facilitate supermassive star formation, as long as the total mass infall rate onto the protostar remains sufficiently high. We extend the analysis further by examining how the abundance of supermassive star candidate haloes would be affected if all haloes with super-critical infall rates, regardless of metallicity were included. We investigate this scenario by identifying all atomic cooling haloes in the Renaissance simulations with central mass infall rates exceeding a fixed threshold. We find that among these haloes with central mass infall rates above $0.1 M_{\odot} \text{ yr}^{-1}$ approximately two-thirds of these haloes have metallicities of $Z > 10^{-3} Z_{\odot}$. If metal mixing within these haloes is inefficient early in their assembly and pockets of metal-poor gas can remain then the number of haloes hosting supermassive stars can be increased by at least a factor of four. Additionally the centres of these high infall-rate haloes provide ideal environments in which to grow pre-existing black holes. Further research into the (supermassive) star formation dynamics of rapidly collapsing haloes, with inhomogeneous metal distributions, is required to gain more insight into both supermassive star formation in early galaxies as well as early black hole growth.

Keywords: Early Universe, Super Massive Stars, Star Formation, First Galaxies, Numerical Methods

1. INTRODUCTION

Supermassive black holes (SMBHs) with masses exceeding $10^9 M_{\odot}$ have long been known to exist at high redshift (e.g. Fan 2001; Dietrich et al. 2002; Fan 2003; Vestergaard 2004; Fan 2004; Fan et al. 2006). The number of quasars, powered by SMBHs, at $z > 6$ now exceeds 200 (Matsuoka et al. 2019)¹ and their number density is estimated to be of order 1 Gpc^{-3} . These 200 or so observed quasars probably represent the tip of the iceberg with many more quasars of lower luminosity (and hence perhaps mass) lurking below the observational threshold of current telescopes.

Nonetheless, the discovery of even this relatively small number of high redshift SMBHs has posed a significant challenge to our understanding of the formation and growth of black holes. Black holes are believed to form as the endpoint of massive stars. The seed black hole may then grow through the accretion of gas or through mergers with other black holes. The significant challenge in this scenario is that SMBHs with masses of up to $10^9 M_{\odot}$ exist (e.g. Bañados et al. 2018) already when the Universe was less than one billion years old. Our current understanding of black hole accretion therefore makes these observations difficult to interpret. Three mainstream scenarios have emerged over the past two decades in an attempt to understand the origin of high- z SMBHs (see Inayoshi et al. 2020 for a recent extended review).

Perhaps the most straightforward scenario is that all black

holes emerge from the end point of the first generation of stars. The initial mass function (IMF) of the first stars is currently unknown, and as yet we have little direct observational guidance. However, simulations, as well as the lack of any observed zero-metallicity stars in our Galaxy, point to an IMF that is top heavy compared to present-day star formation (Yoshida et al. 2006; Turk et al. 2009; Clark et al. 2011; Hirano et al. 2014). While initial studies of Population III (PopIII) star formation concluded that the masses of the first stars were of the order of $100 M_{\odot}$ (Bromm et al. 1999; Abel et al. 2002; Bromm et al. 2002) more recent studies indicate a characteristic mass of a few tens of solar masses but with a range into the hundreds of solar masses (Stacy et al. 2010, 2012; Stacy & Bromm 2014; Hirano et al. 2014, 2015). A black hole born from such stars will have at most the same mass as the progenitor star and hence limited to a few tens to a few hundred solar masses. These black holes are known as “light seeds” (e.g. Volonteri 2010), and will need to increase their mass by up to eight orders of magnitude within a few hundred million years if they are to grow to become a SMBH. Such a scenario has been shown to require substantial fine-tuning (Tanaka & Haiman 2009; Tanaka et al. 2012). Black holes born from PopIII remnants exist in relic ionized regions that are warm and diffuse, inhospitable for growth (Whalen et al. 2004; Milosavljević et al. 2009; Alvarez et al. 2009). Furthermore, after these seeds are incorporated into galaxies, they often find themselves in underdense regions away from the halo centre (Smith et al. 2018). The black holes are unable to grow efficiently and suffer accretion rates orders of magnitudes below the Eddington rate until its host halo is re-

*E-mail: john.regan@mu.ie, Royal Society - SFI University Research Fellow

¹ For recent comprehensive compilations, see Inayoshi et al. (2020) and http://www.sarahbosman.co.uk/list_of_all_quasars.

plenished with gas. Likewise, growing these black holes via mergers is difficult, due to the gravitational-wave recoil which tends to eject the merger remnant from the shallow potential of their host halo (Haiman 2004). It would seem that only in the cases where these black holes can grow at rates significantly exceeding the Eddington limit can these black holes reach sufficiently high masses. While extended episodes of modestly super-Eddington accretion (Madau & Rees 2001; Madau et al. 2014; Alexander & Natarajan 2014; Lupi et al. 2016), as well as shorter episodes of hyper-Eddington accretion (Inayoshi et al. 2016) remain physically viable, it is unclear how often they are realised in nature with a sufficient duty cycle (Pacucci et al. 2017).

Scenarios two and three are the so-called “heavy seed” scenarios, both of which create black holes with initial masses of greater than $1000 M_{\odot}$ and possibly up to $10^6 M_{\odot}$. Scenario two is the collapse of a dense nuclear star cluster (Portegies Zwart et al. 2004; Freitag 2008; Omukai et al. 2008; Devecchi & Volonteri 2009; Merritt 2009; Davies et al. 2011; Lupi et al. 2014). In this case the compact nature of the cluster allows stellar collisions to dominate resulting in the formation of a very massive seed at the centre of the halo. Detailed numerical simulations have been conducted (e.g. Katz et al. 2015; Reinoso et al. 2018; Sakurai et al. 2019) of this scenario and most studies have converged on a final mass of the central object of approximately $1000 M_{\odot}$, constituting a small fraction of the mass of the gas in an atomic-cooling halo. Whether this scenario can ultimately produce SMBHs at early times in the Universe is as of yet unclear and further research of this scenario is still required.

A third scenario, proposed to create yet heavier seeds, is arguably the most well studied. In this scenario very high accretion rates onto embryonic protostars allows for the creation of supermassive stars (SMSs) (Shapiro & Teukolsky 1979; Begelman et al. 2008; Schleicher et al. 2013; Hosokawa et al. 2013; Inayoshi et al. 2014; Sakurai et al. 2016; Umeda et al. 2016; Haemmerlé et al. 2018; Woods et al. 2017, 2019; Regan & Downes 2018b). Haemmerlé et al. (2018) recently found that a mean accretion rate above a critical value of $0.001 M_{\odot} \text{ yr}^{-1}$ is required to create a SMS. If this accretion is maintained, the stellar atmosphere inflates and the star is bloated, causing the surface temperatures to drop to approximately 5000 K (Hosokawa et al. 2013; Woods et al. 2017; Haemmerlé et al. 2018), thus avoiding the deleterious feedback effects from ionizing radiation.

In order to achieve the large required accretion rates, the general assumption has been that a metal-free atomic cooling halo is required, whose gas remains near its virial temperature of $\sim 10^4 \text{ K}$. With the mass accretion rate onto the central regions of a halo scaling as $dM/dt \propto T^{3/2}$ (Shu 1977), such haloes would appear to be optimal regions to support rapid mass infall. The absence of metals removes a cooling pathway for the gas which would otherwise potentially cause the gas to cool and fragment into smaller, lower mass, stars thus preventing the formation of a massive central object. A further criteria is that the atomic cooling halo should have had no previous episode of star formation (which would have internally enriched the halo with metals). In order to maintain the gas temperature near the virial temperature of such a pristine halo, the H_2 content must also be suppressed. Many studies have investigated pathways to achieve this, the main pathways investigated have been to employ strong Lyman-Werner (LW) fluxes (Dijkstra et al. 2008; Shang et al. 2010; Regan et al. 2014; Latif et al. 2014b; Agarwal & Khochfar 2015; Latif

et al. 2015; Regan et al. 2016, 2017; Regan & Downes 2018a), baryonic streaming velocities (Tseliakhovich & Hirata 2010; Tanaka & Li 2014; Hirano et al. 2017; Schauer et al. 2017), collisions of massive proto-galaxies (Mayer et al. 2010, 2015; Inayoshi et al. 2015) and finally dynamical heating caused by a succession of minor and major mergers (Yoshida et al. 2003; Fernandez et al. 2014; Wise et al. 2019).

The goal of the present study is to examine the role that metal enrichment in embryonic haloes may play in the formation of SMSs. We adopt similar terminology from the existing literature on metal-poor stars (e.g. Frebel & Norris 2015). Our definitions differ slightly from those of Frebel & Norris (2015) - particularly by including a “metal-free” category which is generally absent when considering stellar metallicities. We assign the following terms to halo metallicities:

- metal-free $\equiv Z < 10^{-5} Z_{\odot}$
- extremely metal-poor (EMP) $\equiv 10^{-5} Z_{\odot} < Z < 10^{-3} Z_{\odot}$
- metal-enriched² $\equiv Z > 10^{-3} Z_{\odot}$.

The formation of SMSs in haloes with metallicities in the EMP range has recently been investigated by Tagawa et al. (2020) and Chon & Omukai (2020). Tagawa et al. (2020) utilised semi-analytic models, and showed that if the gas fragments at sufficiently high density ($\gtrsim \text{few} \times 10^{10} \text{ cm}^{-3}$), the central protostar avoids contraction and grows via frequent mergers with other protostars into a $\sim 10^5 - 10^6 M_{\odot}$ SMS. This represents a hybrid scenario between the collapse of a dense stellar cluster and the growth of a single SMS discussed above. Chon & Omukai (2020) used high-resolution smoothed particle hydrodynamics simulations to investigate a similar scenario. They followed the cooling, contraction, and fragmentation of gas in the high-density core of a massive halo with a high gas inflow rate ($dM/dt = 1 M_{\odot} \text{ yr}^{-1}$). Chon & Omukai (2020) investigate the effects of both metallicity and dust in their simulations. The impact of dust cooling is investigated using the prescription from Omukai et al. (2008), which operates at gas number densities of $n_{\text{gas}} \gtrsim 10^{10} \text{ cm}^{-3}$. They find that the impact of dust cooling does not extend to scales larger than a few hundred au^3 . Their overall findings are that the formation pathway of massive stars depends strongly on metallicity: the growth of the SMS is dominated by gas accretion in the metal-free case, while mergers with other fragments become dominant as the metallicity approaches the upper limit of the EMP range. They found that SMS formation was prevented at the highest metallicity they studied, $Z = 10^{-3} Z_{\odot}$. However, at all lower metallicities, the end result is the same: the rapid growth of a massive central protostar, at an average rate of $\sim 1 M_{\odot} \text{ yr}^{-1}$.

Overall, the above suggests that *SMS formation in the dense core of an atomic halo is possible, even when it has significant metallicity*, as long as the infall rate is high and fragmentation occurs at sufficiently high density. This raises the question: *how many additional such haloes there are in the early universe, compared to metal-free haloes?* To assess the abundance and demography of such haloes at high redshift, we

² The metal-poor stars community traditionally includes stars with metallicities of $Z > 10^{-3} Z_{\odot}$ in the metal-poor category, but we refer to these stars as metal-enriched, which is more appropriate in the present context.

³ Dust cooling is not included in the Renaissance simulations as we do not reach densities high enough to activate that cooling channel

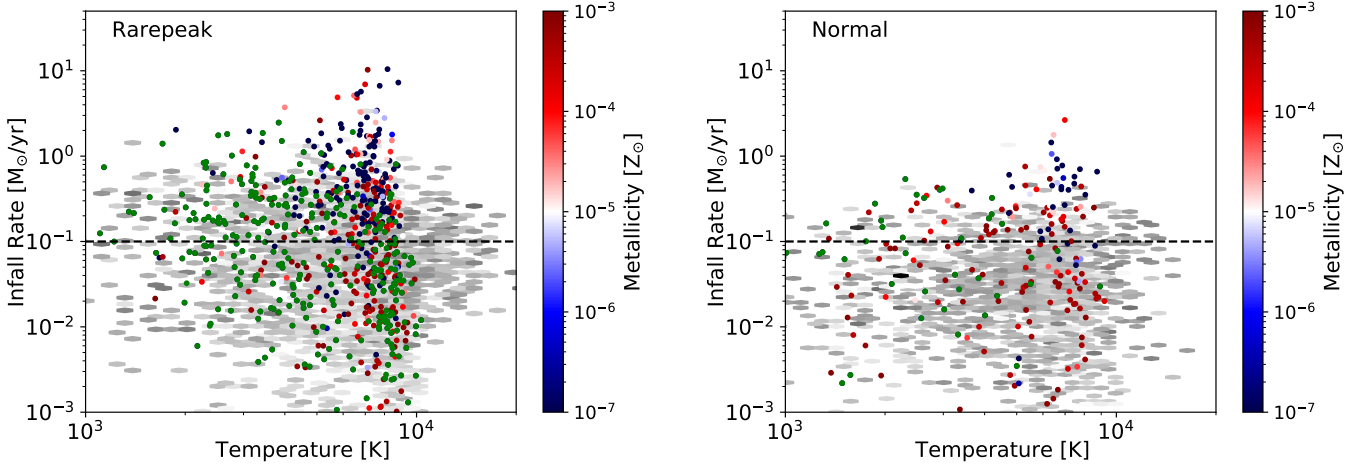


Figure 1. *Left Panel:* The mass infall rate inside 20 pc for all 3244 halos between $15 < z < 24$ in the *Rarepeak* simulation. The infall rates are plotted against the volume averaged temperature of the gas within 20 pc, colour coded by metallicity. Hexbins, in grayscale, are used to represent the metal-enriched haloes ($Z > 10^{-3} Z_{\odot}$). Darker colours signify higher metallicity as well as higher halo counts. Blue, red and green circles represent the lower metallicity haloes. Red circles represent haloes metallicities with $10^{-3} Z_{\odot} \gtrsim Z \gtrsim 10^{-5} Z_{\odot}$ while blue circles represent haloes with $Z \lesssim 10^{-5} Z_{\odot}$. Green circles represent haloes which are both metal-free and star-free. *Right Panel:* The same plot for the 2335 halos between $11.6 < z < 24$ in the *Normal* simulation for the infall rate and temperatures within 20 pc of the halo centres. The *Normal* simulation has fewer very high ($\gtrsim 1 M_{\odot} \text{ yr}^{-1}$) mass infall rate haloes. The majority of haloes in the *Normal* region are also metal-enriched, with fewer extremely metal-poor and metal-free haloes by number (but not by percentage - see Figure 8) compared to the *Rarepeak* region. The black dashed line in each plot marks the $0.1 M_{\odot} \text{ yr}^{-1}$ threshold value. This marks a distinction between high infall rate haloes and lower infall rate haloes.

examine the outputs of the Renaissance Simulations and look for haloes that display rapid collapse, regardless of the metallicity of the halo. We examine rapidly accreting haloes across all redshifts and record their metallicities and other properties. Our analysis expands on similar earlier searches for supermassive star candidate haloes (e.g., Habouzit et al. 2016; Tremmel et al. 2017; Dunn et al. 2018; Wise et al. 2019; Regan et al. 2020) into the regime of haloes that are enriched with metals, selecting candidates based on their infall rates, rather than on the requirement of being metal-free.

This paper is organised as follows. In § 2, we describe the datasets that comprise the Renaissance Simulations and our analysis methods. In § 3, we present our main results, in the form of the demography of haloes with rapid central gas inflow rates, and their distribution in metallicity. Finally, in § 4, we discuss our findings further and summarise the main conclusions and implications of this work.

2. RENAISSANCE DATASETS

The Renaissance Simulations were carried out on the Blue Waters supercomputer facility using the adaptive mesh refinement code *Enzo* (Bryan et al. 2014; Brummel-Smith et al. 2019)⁴. *Enzo* has been extensively used to study the formation of structure in the early universe (Abel et al. 2002; O’Shea et al. 2005; Turk et al. 2012; Wise et al. 2012, 2014; Regan et al. 2015, 2017). In particular, *Enzo* includes a ray-tracing scheme to follow the propagation of radiation from star formation and black hole formation (Wise & Abel 2011) as well as a detailed multi-species chemistry model that tracks the formation and evolution of nine species (Anninos et al. 1997; Abel et al. 1997; Smith et al. 2017). Additionally the photo-dissociation of H_2 is followed, which is a critical ingredient for determining the formation of the first metal-free stars (Haiman et al. 2000).

The datasets used in this study were originally derived

from a simulation of the universe in a $(40 \text{ Mpc})^3$ box using the WMAP7 best fit cosmology (Komatsu et al. 2011). Initial conditions were generated using MUSIC (Hahn & Abel 2011) at redshift $z = 99$. A low-resolution simulation was run until $z = 6$ in order to identify three different regions for re-simulation (Chen et al. 2014). The volume was then smoothed on a physical scale of 5 comoving Mpc, and regions of high ($\langle \delta \rangle \equiv \langle \rho \rangle / (\Omega_M \rho_c) - 1 \simeq 0.68$), average ($\langle \delta \rangle \sim 0.09$), and low ($\langle \delta \rangle \simeq -0.26$) mean overdensity were chosen for re-simulation. These sub-volumes are referred to as the *Rarepeak* region, the *Normal* region and the *Void* region. The *Rarepeak* region has a comoving volume of 133.6 Mpc^3 , and the *Normal* and *Void* regions both have comoving volumes of 220.5 Mpc^3 . Each region was then re-simulated with an effective initial resolution of 4096^3 grid cells and particles within these sub-volumes of the larger initial simulation. This gives a maximum dark matter particle mass resolution of $2.9 \times 10^4 M_{\odot}$. For the re-simulations, further refinement was allowed throughout the sub-volumes up to a maximum refinement level of 12, which corresponds to 19 pc comoving spatial resolution. Given that the *Void*, *Normal* and *Rarepeak* regions focus on different overdensities, each region was evolved forward in time to different epochs. The *Rarepeak* region, being the most overdense and hence the most computationally demanding at earlier times, was run until $z = 15$. The *Normal* region ran until $z = 11.6$, and the *Void* region ran until $z = 8$. In all of the regions the halo mass function was well resolved down to $M_{\text{halo}} \sim 2 \times 10^6 M_{\odot}$. The *Rarepeak* region represents a volume which is 1.68 times denser than the cosmic mean - therefore at $z = 15$, regions with the size and overdensity of the *Rarepeak* are expected to be found in approximately 0.01–0.1% of the volume of the Universe (Wise et al. 2019). Therefore, any results from the *Rarepeak* region need to be viewed in the context of the region being rare ($\sim 10^3 - 10^4$ times rarer than the *Normal* region). The *Rarepeak* regions contains 822 galaxies with masses larger

⁴ <https://enzo-project.org/>

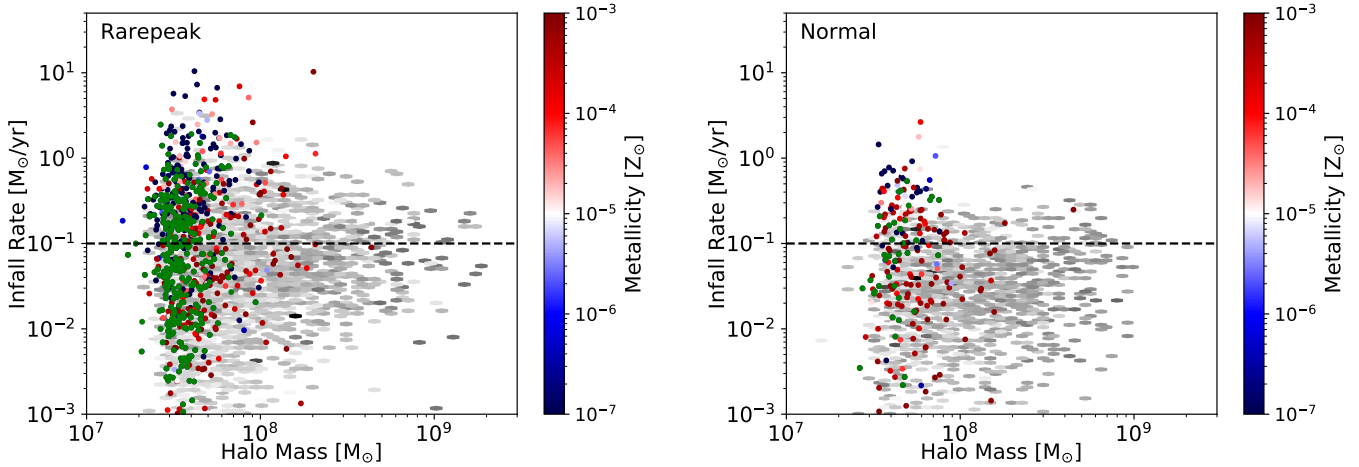


Figure 2. Same as Figure 1, except the infall rates are plotted against the mass of each parent halo. In the *Rarepeak* region (left panel), the extremely metal-poor and metal-free haloes ($Z < 10^{-3} Z_{\odot}$; shown in red and blue colours) populate the halo mass range predominantly just below $10^8 M_{\odot}$. The *Normal* region (right panel) has significantly fewer extremely metal-poor and metal-free haloes in this halo mass range but nonetheless the trend is similar.

than $2 \times 10^7 M_{\odot}$ at $z = 15$, the *Normal* region contains 758 such galaxies at $z = 11.6$, while the *Void* region contains 458 such galaxies at $z = 8$. In this study, we examine only the *Rarepeak* and *Normal* regions. In our previous work (Wise et al. 2019; Regan et al. 2020) we found the *Void* region to be devoid of metal-free and star-free atomic cooling haloes as infall rates did not support their formation, we therefore do not include the *Void* region in this study.

3. RESULTS

3.1. Atomic cooling haloes in the Renaissance simulation

As discussed in §2 the *Rarepeak* dataset represents an overdense region of the Universe with a large selection of galaxies while the *Normal* region represents a region with an average density comparable to the cosmic mean. We begin our analysis of these two datasets by examining only those haloes which lie inside the high-resolution regions and which have masses greater than the atomic cooling limit, which we adopt from Fernandez et al. (2014),

$$M_{\text{atm}} = 2 \times 10^7 \left(\frac{T_{\text{vir}}}{10^4 \text{ K}} \frac{21}{1+z} \right)^{-1.5} M_{\odot}, \quad (1)$$

that is calibrated with simulations, where z is the redshift and T_{vir} is the virial temperature of the halo. We tested other definitions (e.g. Bromm & Yoshida 2011) which give larger values by up to a factor of two or more. The number of metal-free haloes is very sensitive to the chosen value because it lies on the relatively rare exponential part of the halo mass function. We chose a value of the atomic limit consistent with previous work in the literature, and calibrated to correspond to the onset of Lyman α cooling in cosmological simulations, but we note that this choice impacts our results. For both datasets, we then filter each halo based on the mass infall rate in that halo. We calculate the instantaneous mass infall rate using the standard continuity equation:

$$\dot{M} = 4\pi R^2 \rho(R) V_{\text{rad}}(R) \quad (2)$$

where \dot{M} is the mass infall rate, R is the radius at which the infall rate is calculated, $\rho(R)$ is the gas density at that radius and $V_{\text{rad}}(R)$ is the radial velocity at that radius. For both the

Rarepeak and *Normal* region the mass infall rate is calculated as the mean infall rate within 20 pc of the centre of the halo.

The value of 20 pc was dictated by the spatial resolution of our simulations, and was chosen to give a large enough volume over which to calculate the mean while also focusing on the region in which SMS formation is expected.

The *Rarepeak* simulation was run until $z = 15$, but we examine all of the outputs⁵ from the dataset. For the *Normal* datasets we adopt the exact same procedure except that the *Normal* simulation runs until $z = 11.6$ and again we examine all of the outputs⁶. In total, we identified 3,244 atomic cooling haloes across all outputs in the *Rarepeak* region and 2,335 haloes across all outputs in the *Normal* region. These numbers represent haloes at various stages of their growth and accretion rate history.

3.2. Central mass infall rates

We first plot the mass infall rate of each halo against three different halo characteristics. First in Figure 1 we show a scatter plot of the mass infall rates against the inner halo temperature. Secondly in Figure 2 we plot the halo infall rate against the total halo mass, and finally in Figure 3 we show the halo infall rate against the stellar mass of each halo. We begin by analysing Figure 1. In the left panel of Figure 1 we show the results from the *Rarepeak* simulation and in the right panel from the *Normal* simulation. Each point shows the mass infall rate averaged over the inner 20 pc of each atomic cooling halo for the *Rarepeak* and *Normal* region. The mass infall rates are plotted against the average⁷ temperature within the same region in each halo. There are two colour codes on the plot. The grayscale hexbins capture all metallicities⁸ greater than $Z = 10^{-3} Z_{\odot}$. Each coloured circle then refers to the metallicities of the EMP and metal-free haloes. Red circles indicate EMP haloes ($10^{-5} Z_{\odot} \lesssim Z \lesssim 10^{-3} Z_{\odot}$) while blue circles indicate metal-free regions ($Z \lesssim 10^{-5} Z_{\odot}$). We also include green circles on the plot to indicate haloes which are

⁵ There are 40 *Rarepeak* outputs between $z = 24$ and $z = 15$.

⁶ There are 70 *Normal* outputs between $z = 24$ and $z = 11.6$.

⁷ All averages are computed using a cell volume weighted mean

⁸ Note that all metallicities referred to in this paper are gas phase metallicities.

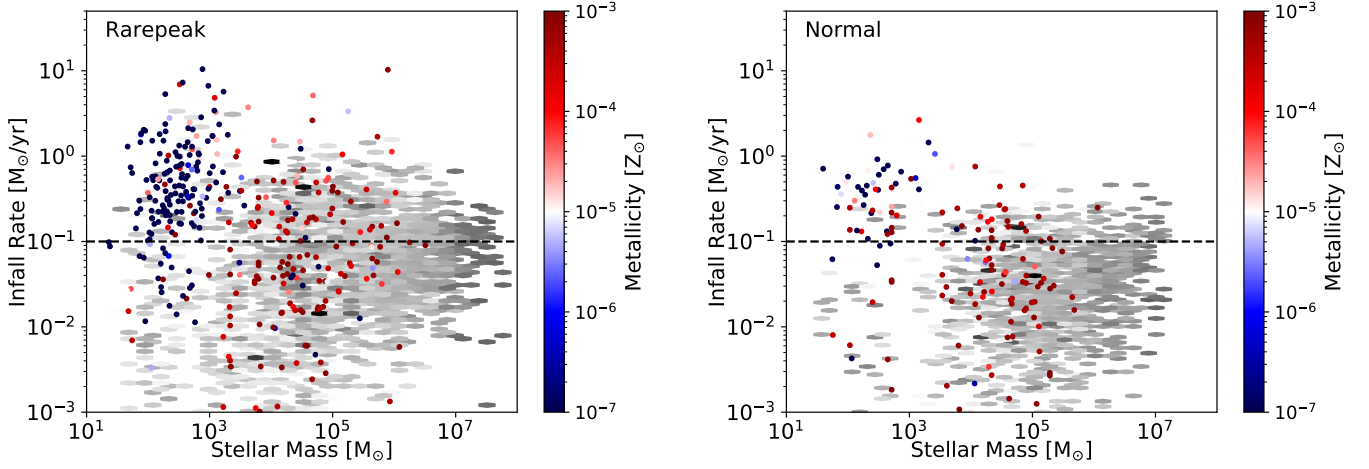


Figure 3. Same as Figures 1 and 2, except the infall rates are plotted against the stellar mass of each parent halo. As can be seen from the *left panel*, the *Rarepeak* region has a large fraction of metal-free haloes residing in low stellar-mass haloes. A substantial fraction of these haloes have high infall rates. The extremely metal poor haloes tend to have larger stellar masses and the metal-enriched haloes more stellar mass still as expected. The *right panel* shows that the *Normal* region has significantly fewer metal-free haloes but that they nonetheless populate the high mass infall region of the plot.

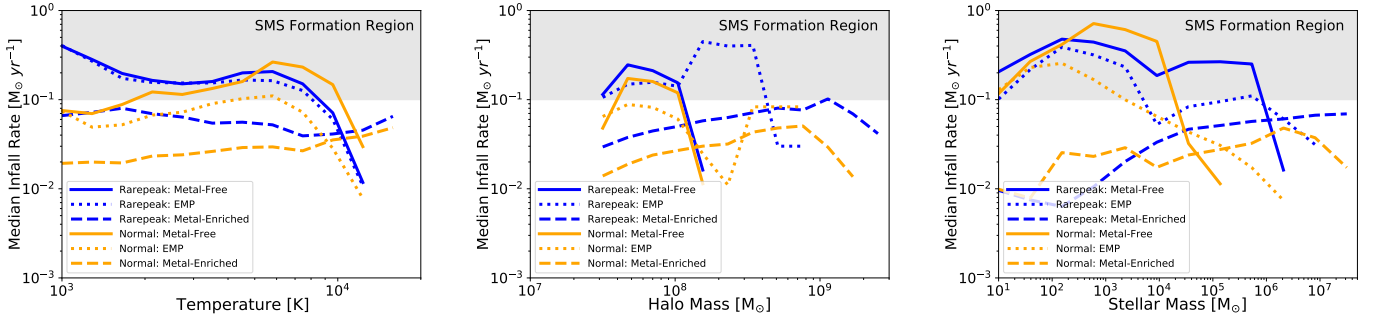


Figure 4. In the three panels, we show how the median infall rate within 20 pc of the centre of each halo varies with temperature (left panel), halo mass (middle panel) and stellar mass (right panel). The metal-free haloes are shown by solid, the EMP haloes by dotted, and the metal-enriched haloes by dashed lines. In all cases the metal-free and EMP haloes show the highest median infall rates for the regions where they exist. The *Rarepeak* region also has systematically higher infall rates compared to the *Normal* region. In each panel, the median rates vary between approximately $0.01 \text{ M}_\odot \text{ yr}^{-1}$ and $1.0 \text{ M}_\odot \text{ yr}^{-1}$. High central infall rates are found in metal-free and EMP haloes clustered around the atomic cooling limit (i.e. a few times 10^7 M_\odot) but towards lower stellar masses. This breakdown of central infall rate by metallicity shows that up to $Z \sim 10^{-3} Z_\odot$ central infall rates are likely to be sufficient to significantly modify the IMF of stars in a halo with the possibility of SMS formation. The grey shaded region above $0.1 \text{ M}_\odot \text{ yr}^{-1}$ signifies the region in which SMS formation may be possible.

metal-free and star-free.

Some results are immediately clear from a comparison of the panels in Figure 1. The *Rarepeak* region clearly has significantly more haloes that have lower metallicities (and/or are metal-free) and it also has more haloes with high infall rates. While this is true by number it is also true by fraction. For the *Rarepeak* region $\sim 25\%$ are classified as EMP or metal-free compared to less than 15% for the *Normal* region. The *Rarepeak* region is also characterised by a large number of rapidly collapsing, EMP and metal-free haloes. The metal-free and star-free haloes (green circles) show a strong scatter and are not preferentially rapid accretors. However, the metal-free and star-free haloes do populate the lower-temperature parts of the phase space. This is because these haloes have no ongoing star formation (by definition) and so the temperature of the gas is determined purely by the competition between gas cooling and dynamical and compressional heating. The other EMP and metal-free haloes, especially those with gas temperatures close to $T = 10^4 \text{ K}$ are being heated by ongoing star formation with atomic line cooling keeping the tempera-

ture close to, or slightly below, $T = 10^4 \text{ K}$. The *Normal* region, as mentioned above, is dominated by metal-enriched haloes with over 85% of haloes being metal-enriched. Furthermore, the fraction of rapidly collapsing haloes is greatly diminished compared to the *Rarepeak* region. In the *Normal* region 10% are rapidly collapsing ($dM/dt > 0.1 \text{ M}_\odot \text{ yr}^{-1}$) compared to 30% for the *Rarepeak* region. In Figure 2 we plot the mass infall rate against the total (dark matter and gas) halo mass. In this representation the EMP and metal-free haloes are strongly clustered, in both the *Rarepeak* and *Normal* regions, at the atomic cooling limit ($M_{\text{atm}} \sim 2 - 5 \times 10^7 \text{ M}_\odot$). This result is not surprising; once the atomic cooling limit is reached, star formation will begin (if it hasn't already), and from that point onwards, it is only a matter of time before the halo becomes metal enriched. There is also a noticeable decline in the number of high infall-rate haloes towards high halo masses. This trend is also seen in Figure 4 (see below). This can be explained through the natural halo merging process where due to the exponential form of the halo mass function smaller haloes are more populous than larger haloes. What we see in Figure

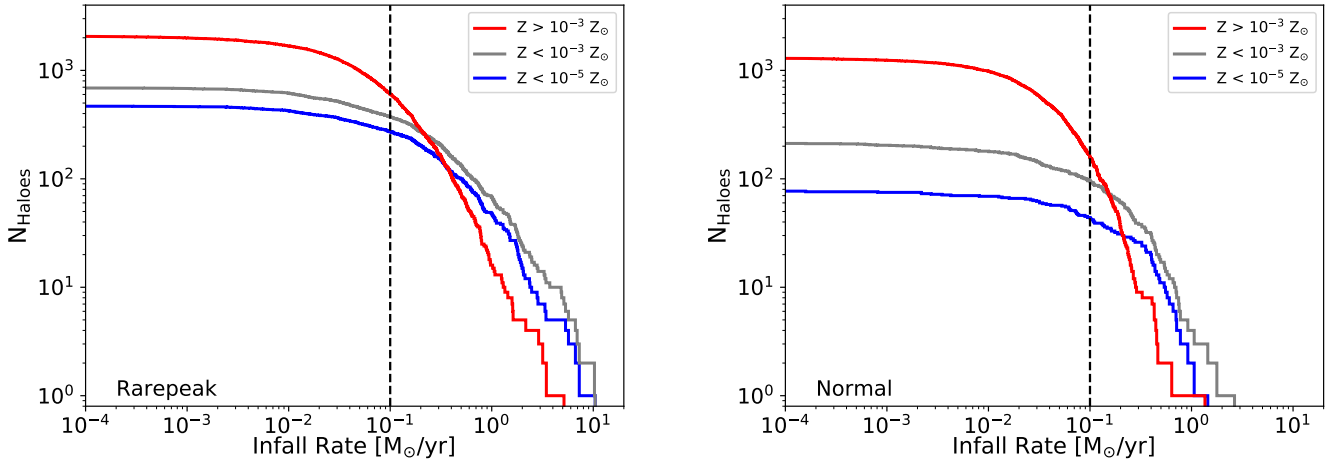


Figure 5. *Left Panel:* The cumulative number of haloes with infall rates greater than the given x-axis value for the *Rarepeak* region. The total number of *Rarepeak* haloes across all outputs is 3,244. Infall rates are again calculated at 20 pc from the halo centre. Haloes are grouped into haloes with metallicities $Z > 10^{-3} Z_{\odot}$ (red line), $Z < 10^{-3} Z_{\odot}$ (grey line) and $Z < 10^{-5} Z_{\odot}$ (blue line). At mass infall rates greater than $0.1 M_{\odot} \text{ yr}^{-1}$, the number of metal-enriched haloes is approximately 2.2 times higher than the number of metal-free haloes ($Z < 10^{-5} Z_{\odot}$). Therefore, if metal-enriched haloes can support SMS formation then the number density of candidate haloes can increase substantially. *Right Panel:* The distribution of infall rates for the *Normal* region. The total number of *Normal* haloes across all outputs is 2,334. In the *Normal* region at mass infall rates greater than $0.1 M_{\odot} \text{ yr}^{-1}$ there is up to a factor of four more metal-enriched haloes compared to metal-free haloes and up to twice as many EMP haloes compared to metal-free haloes.

2 is that mergers of smaller haloes into more massive haloes is driving high mass inflow rates for halos below approximately $10^8 M_{\odot}$. As we increase the mass scale the number (distribution) of haloes becomes smaller (larger) and hence the mass inflow rates decline. This point adds to the fact that haloes just transitioning into the atomic cooling regime are ideal sites for SMS formation.

Complementary to this is Figure 3, where we plot the mass inflow rate against the stellar mass. In the left panel of Figure 3 we show the scatter/hexbin plot, coloured by metallicity, of the *Rarepeak* region. There is a large cluster of metal-free haloes, with $Z \lesssim 10^{-5} Z_{\odot}$, with stellar masses of $M_{*} \lesssim 10^3 M_{\odot}$. These haloes formed PopIII according to the sub-grid PopIII star formation prescription with masses dictated by a pre-defined initial mass function. However, given the rapid inflow rates these haloes could also have formed SMSs had such a sub-grid prescription existed. The haloes are identified here however as their supernovae have not yet fully enriched the halo or the stars have not exploded yet. Allied to this it should also be noted that this group of haloes also contain some of the highest mass inflow rates. With increasing stellar mass the halo metal enrichment levels increase and most EMP haloes are found with stellar masses scattered between $10^3 M_{\odot}$ and $10^6 M_{\odot}$. The metal-free haloes do however have a bias towards higher mass inflow rates compared to the EMP haloes. The *Normal* region contains significantly fewer metal-free haloes and similar to the *Rarepeak* region, the majority have stellar masses with $M_{*} \lesssim 10^3 M_{\odot}$. The overall trend however, while less pronounced than the *Rarepeak* region, is similar.

In Figure 4 we show the median inflow rate for all haloes as a function of temperature, halo mass and stellar mass respectively. Within each panel, the central inflow rates are further broken down according to metallicity. For each case the median inflow rate is calculated as the median inflow rate within 20 pc of the halo centre. To plot the median of all haloes these median values are then binned against temperature, halo mass and stellar mass and the median of each bin again calculated.

Haloes are further subdivided by their metallicity as shown. In each case we see that the *Rarepeak* region has a near systematically higher inflow rate reflecting the more clustered environment of the *Rarepeak* region with mergers and halo interactions more common (Wise et al. 2019; Regan et al. 2020).

However, what is also very noticeable is that the metal-free and EMP haloes have significantly higher central inflow rates compared to the metal-enriched haloes. The high inflow rates suppress early star formation with star formation only taking hold once the halo mass exceeds the atomic cooling limit (see middle panel). The high inflow rate haloes cool in the centre due to H_2 line cooling so their temperatures extend down to 1000 K or below. Many of these (high inflow rate) haloes have small stellar masses peaking around $10^3 M_{\odot}$ (see also Figure 3). A large number of these haloes, with high inflow rates close to the atomic cooling limit, are strong candidates for SMS formation. It should also be noted that at higher halo masses (and stellar masses) that the different metallicity lines essentially converge. The higher halo masses have generally higher metallicities and stellar content. Within these haloes, if SMS formation is to be realised, inhomogeneous pockets of lower metallicity gas will be required.

In summary, from Figures 1, 2 and 3 we see that there exists a sizeable minority of rapidly collapsing haloes which are metal-free ($Z < 10^{-5} Z_{\odot}$). These haloes, due to their large mass inflow rates, makes them strong candidates for super-massive star formation (Woods et al. 2019; Chon & Omukai 2020). However, there exists an even larger population of rapidly collapsing, extremely metal-poor and metal enriched haloes. Some of these haloes could potentially support SMS formation (see e.g. Chon & Omukai 2020), provided the inflow rate does not significantly decrease further inward; and for the metal-enriched haloes if the metal mixing within the halo is inhomogeneous. We will discuss this point further in §4. First we quantify the relative abundance of metal-free, extremely metal-poor and metal-enriched haloes in the next section.

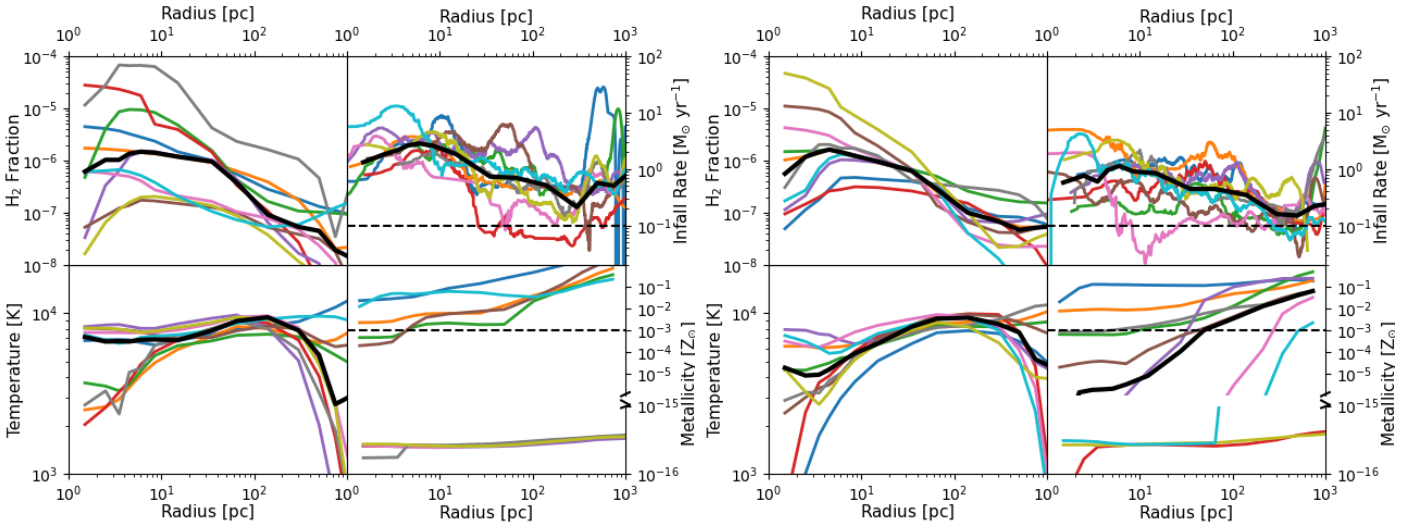


Figure 6. *Left Panel:* Radial profiles for the top 10 highest infall-rate haloes in the *Rarepeak* region. For each halo the temperature, H_2 fraction, infall rate and metallicity are given for each halo. The median radial values for each quantity are shown using the thick black line in each panel. The metallicity (bottom right panel) of haloes can span many orders of magnitude and so that panel is artificially cut in the middle. Nonetheless, what is clear is that the highest infall haloes are evenly spread between those which are metal-free and those which are metal enriched. However, note that even for the metal-enriched haloes the metallicity decreases in all cases towards the halo centre. *Right Panel:* The same plot for the *Normal* haloes. The features are broadly similar, the metallicity sub-panel shows more haloes in transition compared to the *Rarepeak* haloes with a number of haloes showing strongly declining metallicities. Note also that in all cases the haloes have mass infall rates which exceed the critical value for SMS formation of $0.001 M_\odot \text{ yr}^{-1}$ (Haemmerlé et al. 2018) while also exceeding $0.1 M_\odot \text{ yr}^{-1}$ at almost all radii (dashed black line). Note that values of the metallicity (bottom right sub-panel) which fall below $Z \sim 10^{-15} Z_\odot$ should be treated as zero.

3.3. The abundance of metal-free, extremely metal-poor and metal-enriched haloes

In Figure 5 we show the cumulative number of haloes with infall rates greater than the value given on the x-axis. The x-axis runs from $10^{-4} M_\odot \text{ yr}^{-1} \leq \dot{M}(R = 20 \text{ pc}) \leq 10^1 M_\odot \text{ yr}^{-1}$. The mass infall rate, $\dot{M}(R)$, is calculated as the volume averaged value within 20 pc of the centre for both the *Rarepeak* and *Normal* regions. The *Rarepeak* region is shown in the left panel while the *Normal* region is shown in the right panel. Lines in each panel are coloured as follows: red lines are for metal-enriched haloes with metallicities ($Z > 10^{-3} Z_\odot$), grey lines are for haloes with ($Z < 10^{-3} Z_\odot$) and blue lines are for haloes with ($Z < 10^{-5} Z_\odot$).

Concentrating first on the *Rarepeak* region, we see that there are a small number of haloes (84, or 2% of the total) with mass infall rates greater than $1 M_\odot \text{ yr}^{-1}$. Among these (very high-accreting) haloes most are either EMP or metal-free ($\sim 81\%$). However, what is also very relevant from this figure is the number of haloes that occupy the EMP range (i.e. difference in height between the blue and grey lines). If we focus on all haloes with mass infall rates exceeding⁹ $0.1 M_\odot \text{ yr}^{-1}$ then accounting for EMP haloes this increases the number of SMS candidates by a factor of 1.4 and allowing all metal-enriched haloes with mass infall rates greater than $0.1 M_\odot \text{ yr}^{-1}$ increases the number of SMS candidate haloes by more than a factor of two compared to the metal-free case. We will return to this point in §4 below.

In the right panel of Figure 5, we show the same histogram for the *Normal* region. In this case there are two metal-free haloes and two EMP haloes with mass infall rates greater than $1 M_\odot \text{ yr}^{-1}$. There is only a single metal-enriched (with a

metallicity value of $0.0015 Z_\odot$) halo with the same mass infall rate. In the *Normal* region the haloes are dominated by metal-enriched haloes for mass infall rates greater than $0.1 M_\odot \text{ yr}^{-1}$. On the face of it this suggests that the *Normal* region, similar to what was found in the *Rarepeak* region, will support only a small number of supermassive star candidates. However, again if we relax the criteria for supermassive star formation and consider also EMP and metal-enriched haloes then the number of possible candidate haloes can increase by more than a factor of two when we include EMP haloes and up to a factor of four when we include metal-enriched haloes.

In summary what we find is that by including EMP haloes, which Chon & Omukai (2020) and Tagawa et al. (2020) have recently found do support SMS formation, the number of SMS formation haloes can be increased by a factor of at least two. Extending this further to include haloes with metallicities greater than $Z \sim 10^{-3} Z_\odot$ could potentially increase the number of SMS formation sites by a factor of up to four or more compared to the metal-free case. Alternatively, such rapidly collapsing haloes may provide the ideal environment to support the growth of light seed black holes (e.g. Alexander & Natarajan 2014; Inayoshi et al. 2016).

3.4. The Most Rapid Accretors

We next examine the ten most rapidly accreting haloes, when ranked independent of their metallicity, in both simulated regions. In Figure 6 we plot the radial profiles of each of these rapidly accreting haloes. In each panel, we show the temperature, H_2 fraction, mass infall rate and metallicity of each halo as a function of radius. The thick black line in each panel gives the median value for the given quantity. Values across the two panels are broadly similar. Both regions show gas-phase metallicity values that range from completely metal-free ($Z \sim 10^{-16} Z_\odot$) into the metal-free regime and all the way through to those which are metal-enriched ($Z > 10^{-3} Z_\odot$). Note that the metallicity sub-panel of each panel is split between approximately extremely metal-poor and completely

⁹ As previously noted the mass accretion rate onto a protostar must exceed $0.001 M_\odot \text{ yr}^{-1}$ Haemmerlé et al. (2018), however, we choose a threshold here of $0.1 M_\odot \text{ yr}^{-1}$ because we are measuring not the stellar accretion rate but the central mass infall rate at 20 pc.

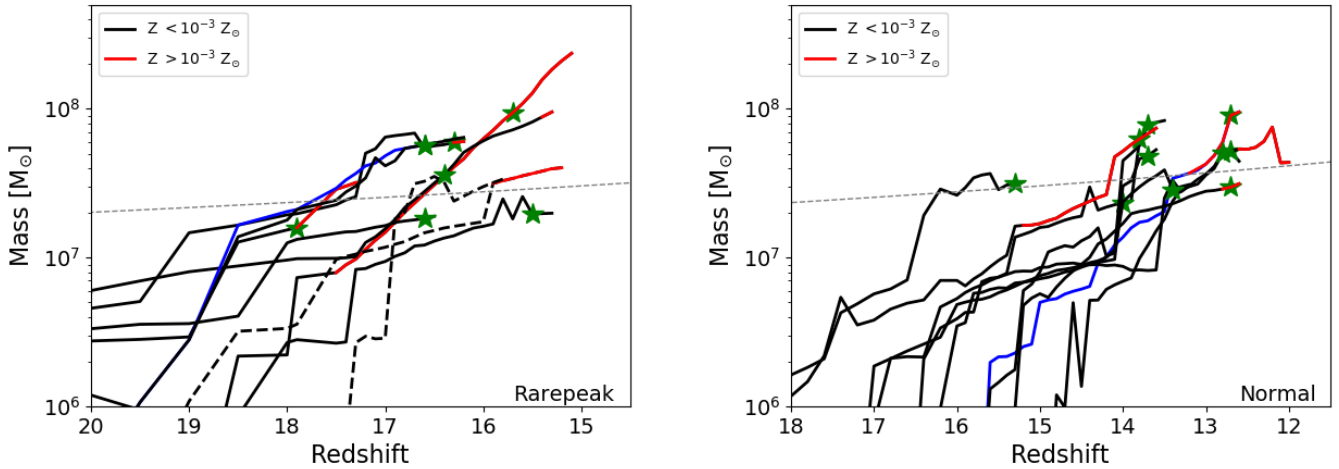


Figure 7. *Left Panel:* The growth rate as a function of redshift for the *Rarepeak* haloes identified in the left panel of Figure 6. Metal-free and extremely metal-poor ($Z < 10^{-3} Z_{\odot}$) haloes are marked in black, while metal-enriched haloes ($Z > 10^{-3} Z_{\odot}$) are marked in red. Note that a halo can exit the metal-free regime during its evolution. The enrichment can come from internal or external sources. Green stars indicate the redshift at which star formation first occurs in each halo. Two haloes have remained star-free until their detection as high infall-rate haloes (indicated by dashed curves). The blue line is the halo which displays the highest instantaneous mass infall rate. The dashed gray near-horizontal line in each panel is the atomic cooling limit. *Right Panel:* The same mass growth plot for the *Normal* region. The trend is similar here with an almost even split between haloes which remain extremely metal-poor or metal-free and those which become enriched. This demonstrates that metal-enriched haloes can have mass infall rates comparable to those which are metal-free all the way into their centre.

metal-free haloes. The dashed line in the metallicity panel indicated the critical metallicity above which SMS formation has been found by Chon & Omukai (2020) to be precluded to occur. Below this line SMS is possible if the accretion rate is sufficient. Note also that each radial profile of each halo’s metallicity shows decreasing metallicity towards the centre of the halo. For some haloes this decrease is highly pronounced, particularly for the *Normal* region. These profiles give some evidence that metal mixing within haloes is likely to be somewhat inhomogeneous and incomplete.

The mass infall rate is shown in the top right panel of each figure. Mass infall rates in both the *Rarepeak* and *Normal* regions, for these select haloes, are comfortably above the critical value thought to be necessary for SMS formation ($0.001 M_{\odot} \text{ yr}^{-1}$; Haemmerlé et al. 2018). The dashed black line marks the value of $0.1 M_{\odot} \text{ yr}^{-1}$ which we use to demarcate very high infall rate haloes. While mass infall rates determined at this radius are in no way a guarantee that this will lead to similar accretion rates onto a protostar, the high rates do suggest that large amounts of matter are being transferred to the halo centre at least.

In Figure 7 we plot the halo mass history of the highest infall-rate haloes shown in Figure 6 with the *Rarepeak* and *Normal* haloes shown on the left- and right-hand panels, respectively. In the panels we identify haloes which are metal-enriched ($Z > 10^{-3} Z_{\odot}$) and those below that threshold. The growth of metal-enriched haloes are marked in red while those below the threshold are marked in black. Note that haloes often transition from EMP/metal-free to metal-enriched during the course of their growth. Haloes can become metal-enriched either through internal star formation and supernovae or alternatively can become metal enriched through external enrichment processes (e.g., Smith et al. 2015). Where star formation first occurs in a halo, the redshift of star formation is denoted by a green star on the halo growth line. Haloes which remain completely star-free are marked as dashed lines. Finally, the blue line denotes the halo which shows the highest instantaneous infall rate in the centre.

In the *Rarepeak* region there are two star-free haloes. One of these haloes becomes metal-enriched, although it has yet to form a star by the time the halo is detected as a high infall-rate halo. The time of metal enrichment compared to star formation is somewhat varied between haloes. Some haloes form stars and then metal-enrichment follows (internal enrichment). In other cases, metal-enrichment precedes star formation, as noted above. However, given that these galaxies have deeper potential wells and longer sound crossing times, the metal mixing can be gradual in some haloes but more rapid in others as was shown in Figure 6. The *Normal* region haloes in the right hand panel show similar trends. The *Normal* region has no star-free haloes, with all haloes in this subset undergoing at least some star formation.

4. DISCUSSION AND CONCLUSIONS

The goal of this paper is to examine the prevalence of high infall-rate halos in the Renaissance Simulations, which in turn are thought to accurately represent early structure formation in our Universe (Chen et al. 2014; Xu et al. 2013, 2014; O’Shea et al. 2015; Barrow et al. 2017; Wise et al. 2019). A high mass accretion rate onto an embryonic protostar is thought to be the single most important criterion for the formation of a SMS (Hosokawa et al. 2013; Sakurai et al. 2016; Woods et al. 2019; Haemmerlé et al. 2018). Therefore, we examine the Renaissance datasets for haloes which are experiencing rapid gas inflow in their centres. While rapid gas inflow to the halo centre, measured at 20 pc from the centre, in order to ensure good cell sampling, does not guarantee that a SMS will ultimately form, it is very likely to be a necessary condition.

Previous investigations of SMS candidate haloes¹⁰ have almost universally focused on metal-free haloes in which the

¹⁰ These haloes are often referred to as “direct collapse black hole” host haloes in the literature due to the fact that the high infall rates are thought to lead to massive black hole formation in certain circumstances. However, current research indicates that the intermediary stage involves a SMS, with no supernova event, and hence we use that terminology here.

equation of state of the gas was determined by the gas phase cooling mechanisms of hydrogen and helium. Here, we extend the analysis to haloes that are either extremely metal-poor ($10^{-3} Z_{\odot} < Z < 10^{-5} Z_{\odot}$) or metal-enriched ($Z > 10^{-3} Z_{\odot}$). If the number density of haloes that support SMS formation can be extended to include non metal-free haloes (at least perhaps up to some metallicity or due to metal enrichment inhomogeneity) then the number density of candidate SMS host haloes will increase accordingly, and so is of immense interest to the community. Previous SMS candidate halo number densities, including metal-free haloes only, have tended to show that the number of SMS candidate haloes may be just sufficient to explain the number density of high- z quasars, not leaving much room to lose a large fraction of these candidates (Agarwal et al. 2012; Visbal et al. 2014; Agarwal et al. 2016; Latif et al. 2014a; Valiante et al. 2016; Habouzit et al. 2016; Valiante et al. 2017; Habouzit et al. 2017; Regan et al. 2017).

Chon & Omukai (2020) have recently shown, through dedicated high-resolution numerical simulations of the collapse of candidate SMS haloes that metallicities with $Z < 10^{-3} Z_{\odot}$ are compatible with SMS formation. They showed that for metallicities of $Z \lesssim 5 \times 10^{-5} Z_{\odot}$ the behaviour of SMS formation is the same as the metal-free case, i.e. SMS formation results directly from the rapid accretion of pristine gas. Chon & Omukai (2020) further showed that when the metallicity enters the extremely metal-poor regime, $5 \times 10^{-5} Z_{\odot} < Z < 10^{-3} Z_{\odot}$, then while the gas does fragment, the fragments nonetheless coalesce onto the growing protostar and the result is a SMS. Tagawa et al. (2020) came to similar conclusions using a semi-analytic approach (see also Inayoshi & Haiman 2014 for similar conclusions in the case of a fragmenting disc in an atomic-cooling halo). In the case of higher metal enrichment, $Z \gtrsim 10^{-3} Z_{\odot}$, Chon & Omukai (2020) find that gas cooling becomes too rapid and the gas fragments into low-mass fragments and SMS formation is inhibited. However, there remains the possibility even in these metal-enriched haloes that pockets of metal-poor gas will remain in which SMS formation can occur. The topic of metal inhomogeneity was outside the scope of Chon & Omukai (2020) but given that metal mixing has previously been shown to have very strong mixing gradients in haloes in the early universe (e.g. Smith et al. 2015) this (metal-enriched) scenario warrants further research, similar to what Tarumi et al. (2020) have done in the context of stellar archaeology where they looked at the difference in metal mixing between internally and externally enriched galaxies.

With this in mind, we included all rapidly collapsing haloes in our analysis, regardless of metallicity. To do this, we examined the Renaissance datasets, analysing both the *Normal* and *Rarepeak* regions. We analysed the simulation volumes and filtered atomic cooling haloes by their instantaneous mass infall rates, averaged within 20 pc of the centre of each halo.

We found that, as expected, there is a large number of haloes with very high central infall rates (see Fig. 5). At infall rates greater than $1 M_{\odot} \text{ yr}^{-1}$ the fraction of rapidly collapsing haloes are dominated by haloes with metallicities less than $10^{-3} Z_{\odot}$ ($\sim 81\%$). Relaxing the mass infall criteria to $0.1 M_{\odot} \text{ yr}^{-1}$, we find that among these “high-accreting” haloes, the majority are either metal-enriched ($Z > 10^{-3} Z_{\odot}$) or extremely metal-poor ($10^{-5} Z_{\odot} < Z < 10^{-3} Z_{\odot}$).

In Figure 8 we show the fraction of high accretion rate ($\dot{M} > 0.1 M_{\odot} \text{ yr}^{-1}$) haloes and their (gas phase) metallic-

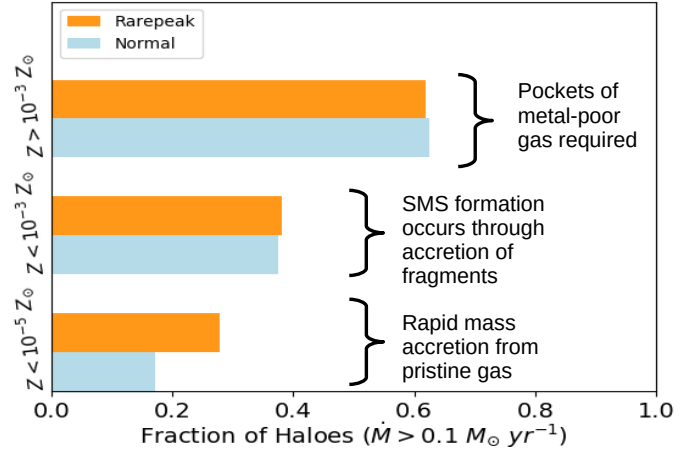


Figure 8. The fraction of haloes which have metallicities of $Z > 10^{-3} Z_{\odot}$, $Z < 10^{-3} Z_{\odot}$ and $Z < 10^{-5} Z_{\odot}$ and have mass infall rates greater than $0.1 M_{\odot} \text{ yr}^{-1}$. *Rarepeak* haloes are coloured in orange. *Normal* haloes in blue. The majority of haloes in both cases are metal enriched and hence within those haloes pockets of extremely metal-poor gas is likely required, including on scales below those resolved here, for SMSs to form.

ities for haloes from both the *Normal* and *Rarepeak* simulations. The *Rarepeak* haloes are displayed in orange, the *Normal* haloes in blue. For the *Rarepeak* region the majority (62%) are metal-enriched (i.e. $Z > 10^{-3} Z_{\odot}$) with 38% extremely metal-poor or metal-free. For the *Normal* region the fractions are very similar. Since the *Normal* region represents a typical region of the Universe, the results for the *Normal* region can be assumed representative of regions likely to be observed, at least by upcoming wide-field surveys (although not quite reaching yet the high redshifts probed in this study, e.g. Nancy Grace Roman Space Telescope and Euclid). While a comprehensive study of the number density of SMS candidate haloes is outside the scope of the present paper, we estimate the number density of SMS candidate haloes as a function of metallicity by examining the final snapshots for the *Rarepeak* and *Normal* simulations. If we again consider haloes with central mass infall rates greater than $0.1 M_{\odot} \text{ yr}^{-1}$, then we find that for the *Rarepeak* region the number density of metal-free haloes is 0.26 cMpc^{-3} . Including the EMP haloes increases the number density to 0.35 cMpc^{-3} . Recall that the *Rarepeak* environment is a biased region and so the number densities found here should be multiplied by a factor between $10^{-3} - 10^{-4}$ to account for this bias (Wise et al. 2019). Doing this we find a number density of approximately $10^{-5} \text{ cMpc}^{-3}$ as a global estimate. This number density is nonetheless orders of magnitude above the observed number density of SMBHs at $z = 6$ (number density $\sim 1 \text{ cGpc}^{-3}$). We are currently investigating the wider number density implication of our calculations (Arridge et al. in prep) but this preliminary result confirms and reinforces the result found in Wise et al. (2019) that there is likely to be a large population of faint quasars/intermediate mass black holes at high redshifts.

In the optimistic case, where all of these metal-enriched haloes support SMS formation, the boost to candidate haloes for SMS formation, compared to the metal-free case, can be increased by a factor of at least four. Some of these haloes may ultimately be shown through both higher-resolution simulations and through considering additional physics (e.g. dust and gas opacity) to not support SMS formation. Neverthe-

less, their high mass infall rates will, at a minimum, transfer a large amount of baryons towards the halo centre, which may impact the initial mass function and is worth further investigation. Furthermore, such high-infall rate haloes may support the rapid growth of less massive, pre-existing, black holes.

Additional high-resolution hydrodynamic simulations will be required to determine the fraction of metal-enriched haloes which can support SMS formation, and, in particular, whether the accretions rates in the cores remain sufficiently high. This could occur if pockets of metal-poor gas in the cores of these haloes remain, allowing rapid accretion and supporting SMS formation. There are clear indications from our analysis of the radial metallicity profiles (see Figure 6) that metal mixing decreases strongly towards the halo centre. We ran an additional analysis of the SMS candidate haloes using a narrower prescription for the radius at which we calculate the accretion rates and the metallicity. Using a radius of 10 pc from the centre the number of EMP and metal-free haloes detected increases to 58% up from 38% reflecting the strong metallicity gradient found in most haloes. If this mixing inefficiency persists to even smaller radii (which it appears to), then metal inhomogeneity may be common in the cores of these young proto-galaxies. The galaxies studied here are embryonic and have had very few dynamical times in which gas mixing can take place and hence extremely metal-poor pockets are much more likely here than in more mature and evolved galaxies at lower redshift.

The addition of extremely metal-poor and metal-enriched haloes to the number density of SMS candidate haloes would help relieve the current tensions that exist in understanding the formation pathways for high- z quasars. More generally, they could significantly modify the “initial mass function” of the earliest supermassive black holes.

ACKNOWLEDGMENTS

JR acknowledges support from the Royal Society and Science Foundation Ireland under grant number URF\R1\191132. ZH acknowledges support from NASA grant NNX15AB19G and National Science Foundation grant AST-1715661. JHW is supported by National Science Foundation grants AST-1614333 and OAC-1835213, and NASA grants NNX17AG23G and 80NSSC20K0520. BWO acknowledges support from NSF grants PHY-1430152, AST-1514700, AST-1517908, and OAC-1835213, by NASA grants NNX12AC98G and NNX15AP39G, and by HST-AR-13261 and HST-AR-14315. The Renaissance simulations were performed on Blue Waters, which is operated by the National Center for Supercomputing Applications (NCSA) with PRAC allocation support by the NSF (awards ACI-1238993, ACI-1514580, and OAC-1810584). This research is part of the Blue Waters sustained-petascale computing project, which is supported by the NSF (awards OCI-0725070, ACI-1238993) and the state of Illinois. Blue Waters is a joint effort of the University of Illinois at Urbana-Champaign and its NCSA. The freely available plotting library MATPLOTLIB (Hunter 2007) was used to construct numerous plots within this paper. Computations and analysis described in this work were performed using the publicly-available *Enzo* (Bryan et al. 2014; Brummel-Smith et al. 2019) and *y_t* (Turk et al. 2011) codes, which are the product of a collaborative effort of many independent scientists from numerous institutions around the world. Their commitment to open science has helped make this work possible. Finally, the authors would like to thank the anonymous referee whose comments greatly

improved the final manuscript.

REFERENCES

- Abel T., Anninos P., Zhang Y., Norman M. L., 1997, *New Astronomy*, 2, 181
 Abel T., Bryan G. L., Norman M. L., 2002, *Science*, 295, 93
 Agarwal B., Khochfar S., 2015, *MNRAS*, 446, 160
 Agarwal B., Khochfar S., Johnson J. L., Neistein E., Dalla Vecchia C., Livio M., 2012, *MNRAS*, 425, 2854
 Agarwal B., Smith B., Glover S., Natarajan P., Khochfar S., 2016, *MNRAS*, 459, 4209
 Alexander T., Natarajan P., 2014, *Science*, 345, 1330
 Alvarez M. A., Wise J. H., Abel T., 2009, *ApJ*, 701, L133
 Anninos P., Zhang Y., Abel T., Norman M. L., 1997, *New Astronomy*, 2, 209
 Bañados E. et al., 2018, *Nature*, 553, 473
 Barrow K. S. S., Wise J. H., Norman M. L., O’Shea B. W., Xu H., 2017, *MNRAS*, 469, 4863
 Begelman M. C., Rossi E. M., Armitage P. J., 2008, *MNRAS*, 387, 1649
 Bromm V., Yoshida N., 2011, *ARA&A*, 49, 373
 Bromm V., Coppi P. S., Larson R. B., 1999, *ApJ*, 527, L5
 Bromm V., Coppi P. S., Larson R. B., 2002, *ApJ*, 564, 23
 Brummel-Smith C. et al., 2019, *The Journal of Open Source Software*, 4, 1636
 Bryan G. L., Norman M. L., O’Shea B. W., Abel T., Wise J. H., Turk M. J., The Enzo Collaboration, 2014, *ApJS*, 211, 19
 Chen P., Wise J. H., Norman M. L., Xu H., O’Shea B. W., 2014, *ApJ*, 795, 144
 Chon S., Omukai K., 2020, *MNRAS*
 Clark P. C., Glover S. C. O., Smith R. J., Greif T. H., Klessen R. S., Bromm V., 2011, *Science*, 331, 1040
 Davies M. B., Miller M. C., Bellovary J. M., 2011, *ApJ*, 740, L42
 Devecchi B., Volonteri M., 2009, *ApJ*, 694, 302
 Dietrich M., Hamann F., Shields J. C., Constantin A., Vestergaard M., Chaffee F., Foltz C. B., Junkkarinen V. T., 2002, *ApJ*, 581, 912
 Dijkstra M., Haiman Z., Mesinger A., Wyithe J. S. B., 2008, *MNRAS*, 391, 1961
 Dunn G., Bellovary J., Holley-Bockelmann K., Christensen C., Quinn T., 2018, *ApJ*, 861, 39
 Fan X. et al., 2006, *AJ*, 131, 1203
 Fan X. e. a., 2001, *AJ*, 122, 2833
 Fan X. e. a., 2003, *AJ*, 125, 1649
 Fan X. e. a., 2004, *AJ*, 128, 515
 Fernandez R., Bryan G. L., Haiman Z., Li M., 2014, *MNRAS*, 439, 3798
 Frebel A., Norris J. E., 2015, *ARA&A*, 53, 631
 Freitag M., 2008, in H. Beuther, H. Linz, T. Henning, eds, *Massive Star Formation: Observations Confront Theory*. Astronomical Society of the Pacific Conference Series, Vol. 387, pp. 247–+
 Habouzit M., Volonteri M., Latif M., Dubois Y., Peirani S., 2016, *MNRAS*, 463, 529
 Habouzit M., Volonteri M., Dubois Y., 2017, *MNRAS*, 468, 3935
 Haemmerlé L., Woods T. E., Klessen R. S., Heger A., Whalen D. J., 2018, *MNRAS*, 474, 2757
 Hahn O., Abel T., 2011, *MNRAS*, 415, 2101
 Haiman Z., 2004, *ApJ*, 613, 36
 Haiman Z., Abel T., Rees M. J., 2000, *ApJ*, 534, 11
 Hirano S., Hosokawa T., Yoshida N., Umeda H., Omukai K., Chiaki G., Yorke H. W., 2014, *ApJ*, 781, 60
 Hirano S., Hosokawa T., Yoshida N., Omukai K., Yorke H. W., 2015, *MNRAS*, 448, 568
 Hirano S., Hosokawa T., Yoshida N., Kuiper R., 2017, *Science*, 357, 1375
 Hosokawa T., Yorke H. W., Inayoshi K., Omukai K., Yoshida N., 2013, *ApJ*, 778, 178
 Hunter J. D., 2007, *Computing in Science & Engineering*, 9, 90
 Inayoshi K., Haiman Z., 2014, *MNRAS*, 445, 1549
 Inayoshi K., Omukai K., Tasker E., 2014, *MNRAS*, 445, L109
 Inayoshi K., Visbal E., Kashiyama K., 2015, *MNRAS*, 453, 1692
 Inayoshi K., Haiman Z., Ostriker J. P., 2016, *MNRAS*, 459, 3738
 Inayoshi K., Visbal E., Haiman Z., 2020, *ARA&A*, in press; e-print arXiv:1911.05791, arXiv:1911.05791
 Katz H., Sijacki D., Haehnelt M. G., 2015, *MNRAS*, 451, 2352
 Komatsu E. et al., 2011, *ApJS*, 192, 18
 Latif M. A., Bovino S., Van Borm C., Grassi T., Schleicher D. R. G., Spaans M., 2014a, *MNRAS*, 443, 1979
 Latif M. A., Schleicher D. R. G., Bovino S., Grassi T., Spaans M., 2014b, *ApJ*, 792, 78
 Latif M. A., Bovino S., Grassi T., Schleicher D. R. G., Spaans M., 2015, *MNRAS*, 446, 3163

- Lupi A., Colpi M., Devecchi B., Galanti G., Volonteri M., 2014, MNRAS, 442, 3616
- Lupi A., Haardt F., Dotti M., Fiacconi D., Mayer L., Madau P., 2016, MNRAS, 456, 2993
- Madau P., Rees M. J., 2001, ApJ, 551, L27
- Madau P., Haardt F., Dotti M., 2014, ApJ, 784, L38
- Matsuoka Y. et al., 2019, ApJ, 883, 183
- Mayer L., Kazantzidis S., Escala A., Callegari S., 2010, Nature, 466, 1082
- Mayer L., Fiacconi D., Bonoli S., Quinn T., Roškar R., Shen S., Wadsley J., 2015, ApJ, 810, 51
- Merritt D., 2009, ApJ, 694, 959
- Milosavljević M., Couch S. M., Bromm V., 2009, ApJ, 696, L146
- Omukai K., Schneider R., Haiman Z., 2008, ApJ, 686, 801
- O'Shea B. W., Abel T., Whalen D., Norman M. L., 2005, ApJ, 628, L5
- O'Shea B. W., Wise J. H., Xu H., Norman M. L., 2015, ApJ, 807, L12
- Pacucci F., Natarajan P., Volonteri M., Cappelluti N., Urry C. M., 2017, ApJ, 850, L42
- Portegies Zwart S. F., Baumgardt H., Hut P., Makino J., McMillan S. L. W., 2004, Nature, 428, 724
- Regan J. A., Downes T. P., 2018a, MNRAS, 475, 4636
- Regan J. A., Downes T. P., 2018b, MNRAS, 478, 5037
- Regan J. A., Johansson P. H., Wise J. H., 2014, ApJ, 795, 137
- Regan J. A., Johansson P. H., Wise J. H., 2015, MNRAS, 449, 3766
- Regan J. A., Johansson P. H., Wise J. H., 2016, MNRAS
- Regan J. A., Visbal E., Wise J. H., Haiman Z., Johansson P. H., Bryan G. L., 2017, Nature Astronomy, 1, 0075
- Regan J. A., Wise J. H., O'Shea B. W., Norman M. L., 2020, MNRAS, 492, 3021
- Reinoso B., Schleicher D. R. G., Fellhauer M., Klessen R. S., Boekholt T. C. N., 2018, A&A, 614, A14
- Sakurai Y., Vorobyov E. I., Hosokawa T., Yoshida N., Omukai K., Yorke H. W., 2016, MNRAS, 459, 1137
- Sakurai Y., Yoshida N., Fujii M. S., 2019, MNRAS, 484, 4665
- Schauer A. T. P., Regan J., Glover S. C. O., Klessen R. S., 2017, MNRAS, 471, 4878
- Schleicher D. R. G., Palla F., Ferrara A., Galli D., Latif M., 2013, A&A, 558, A59
- Shang C., Bryan G. L., Haiman Z., 2010, MNRAS, 402, 1249
- Shapiro S. L., Teukolsky S. A., 1979, ApJ, 234, L177
- Shu F. H., 1977, ApJ, 214, 488
- Smith B. D., Wise J. H., O'Shea B. W., Norman M. L., Khochfar S., 2015, MNRAS, 452, 2822
- Smith B. D., Regan J. A., Downes T. P., Norman M. L., O'Shea B. W., Wise J. H., 2018, MNRAS, 480, 3762
- Smith B. D. et al., 2017, MNRAS, 466, 2217
- Stacy A., Bromm V., 2014, ApJ, 785, 73
- Stacy A., Greif T. H., Bromm V., 2010, MNRAS, 403, 45
- Stacy A., Greif T. H., Bromm V., 2012, MNRAS, 422, 290
- Tagawa H., Haiman Z., Kocsis B., 2020, ApJ, 892, 36
- Tanaka T., Haiman Z., 2009, ApJ, 696, 1798
- Tanaka T., Perna R., Haiman Z., 2012, MNRAS, 425, 2974
- Tanaka T. L., Li M., 2014, MNRAS, 439, 1092
- Tarumi Y., Hartwig T., Magg M., 2020, ApJ, 897, 58
- Tremmel M., Karcher M., Governato F., Volonteri M., Quinn T. R., Pontzen A., Anderson L., Bellovary J., 2017, MNRAS, 470, 1121
- Tselikhovich D., Hirata C., 2010, Phys. Rev. D, 82, 083520
- Turk M. J., Abel T., O'Shea B., 2009, Science, 325, 601
- Turk M. J., Smith B. D., Oishi J. S., Skory S., Skillman S. W., Abel T., Norman M. L., 2011, ApJS, 192, 9
- Turk M. J., Oishi J. S., Abel T., Bryan G. L., 2012, ApJ, 745, 154
- Umeda H., Hosokawa T., Omukai K., Yoshida N., 2016, ApJ, 830, L34
- Valiante R., Schneider R., Volonteri M., Omukai K., 2016, MNRAS, 457, 3356
- Valiante R., Agarwal B., Habouzit M., Pezzulli E., 2017, PASA, 34, e031
- Vestergaard M., 2004, ApJ, 601, 676
- Visbal E., Haiman Z., Bryan G. L., 2014, MNRAS, 445, 1056
- Volonteri M., 2010, A&A Rev., 18, 279
- Whalen D., Abel T., Norman M. L., 2004, ApJ, 610, 14
- Wise J. H., Abel T., 2011, MNRAS, 414, 3458
- Wise J. H., Turk M. J., Norman M. L., Abel T., 2012, ApJ, 745, 50
- Wise J. H., Demchenko V. G., Halicek M. T., Norman M. L., Turk M. J., Abel T., Smith B. D., 2014, MNRAS, 442, 2560
- Wise J. H., Regan J. A., O'Shea B. W., Norman M. L., Downes T. P., Xu H., 2019, Nature, 566, 85
- Woods T. E., Heger A., Whalen D. J., Haemmerlé L., Klessen R. S., 2017, ApJ, 842, L6
- Woods T. E. et al., 2019, PASA, 36, e027
- Xu H., Wise J. H., Norman M. L., 2013, ApJ, 773, 83
- Xu H., Ahn K., Wise J. H., Norman M. L., O'Shea B. W., 2014, ApJ, 791, 110
- Yoshida N., Abel T., Hernquist L., Sugiyama N., 2003, ApJ, 592, 645
- Yoshida N., Omukai K., Hernquist L., Abel T., 2006, ApJ, 652, 6

This paper was built using the Open Journal of Astrophysics L^AT_EX template. The OJA is a journal which provides fast and easy peer review for new papers in the `astro-ph` section of the arXiv, making the reviewing process simpler for authors and referees alike. Learn more at <http://astro.theoj.org>.